nature biomedical engineering

SUPPLEMENTARY INFORMATION

VOLUME: 1 | ARTICLE NUMBER: 0071

In the format provided by the authors and unedited.

Single-impulse Panoramic Photoacoustic Computed Tomography of Small-animal Whole-body Dynamics at High Spatiotemporal Resolution

Lei Li[1, 2†], Liren Zhu[2, 3†], Cheng Ma[3, 4†], Li Lin[2, 3†], Junjie Yao[3, 5], Lidai Wang[3, 6], Konstantin Maslov[2], Ruiying Zhang[3], Wanyi Chen[3], Junhui Shi[2], Lihong V. Wang[2, 7*]

[1]*Department of Electrical and Systems Engineering, Washington University in St. Louis, One Brookings Dr., St. Louis, MO, 63130.*

[2]*Department of Medical Engineering, California Institute of Technology, 1200 E California Blvd., Pasadena, CA 91125.*

[3]*Department of Biomedical Engineering, Washington University in St. Louis, One Brookings Dr., St. Louis, MO, 63130.*

[4]*Present address: Department of Electronic Engineering, Tsinghua University, Beijing, 100084, China.*

[5]*Present address: Department of Biomedical Engineering, Duke University, Durham, NC, 27708.*

[6]*Present address: Department of Mechanical and Biomedical Engineering, City University of Hong Kong, Kowloon, Hong Kong, China.*

[7] *Department of Electrical Engineering, California Institute of Technology, 1200 E California Blvd., Pasadena, CA 91125*

*Correspondence to: L.V.W. (LVW@Caltech.edu).

†These authors contributed equally.

Supplementary Materials

Supplementary Table

Table 1. Comparison of SIP-PACT and state-of-the-art small-animal PACT

	SIP-PACT	State-of-the-art PACT[1-4]
Light delivery	**Free-space delivery**: practically unlimited delivered pulse energy (high sensitivity while complying with ANSI regulation) and uniform illumination (minimized image artifacts)	**Fiber delivery**: limited delivered pulse energy and nonuniform illumination
Detection coverage	**2π**: full-view fidelity	**(3/2)π**: missed features and induced reconstruction artifacts
512-channel acoustic detection	**Yes**: above the spatial Nyquist sampling frequency for *scan-free* cross-sectional whole-body small-animal imaging	**Yes**: but below the spatial Nyquist sampling frequency for *scan-free* 3D whole-body small-animal imaging
Pre-amplification	**Yes**: dominance over cable-transmission noise	**No**
512-channel parallel digitization	**Yes**: single impulse data acquisition without motion artifacts	**Yes**
Reconstruction	**Half-time and dual-speed-of-sound universal back-projection**: minimization of reconstruction artifacts induced by acoustic heterogeneity	**Full-time and single-speed-of-sound reconstruction**: no correction for acoustic heterogeneity
Single-impulse sensitivity	**High due to the combination of the above factors**: high-resolution imaging of small features at depths	**Low**
Frame rate	**50 Hz**: above the Nyquist sampling rate for small-animal heartbeat (5–14 Hz)[5] imaging	**10 Hz**: below the Nyquist sampling rate for small-animal heartbeat imaging
Anatomical imaging	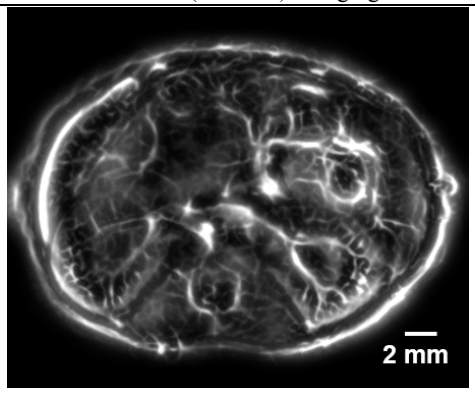 Clearly shows detailed structures and vasculatures of deeply located internal organs in an *adult* mouse	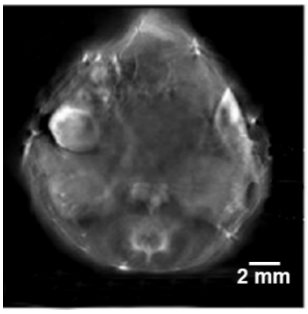 Barely differentiates internal organs in an *immature* mouse
Arterial network mapping	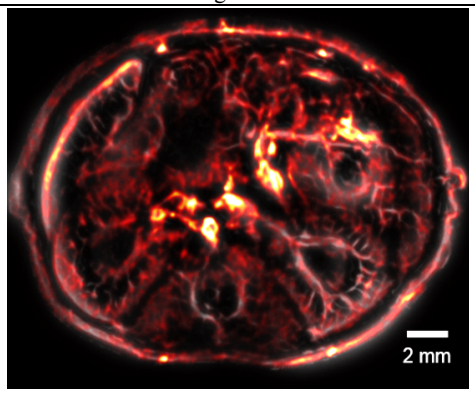 Identifies the arterial network in a mouse whole-body cross-sectional image by heartbeat encoding	Not demonstrated

Measurement of arterial pulse wave phase difference	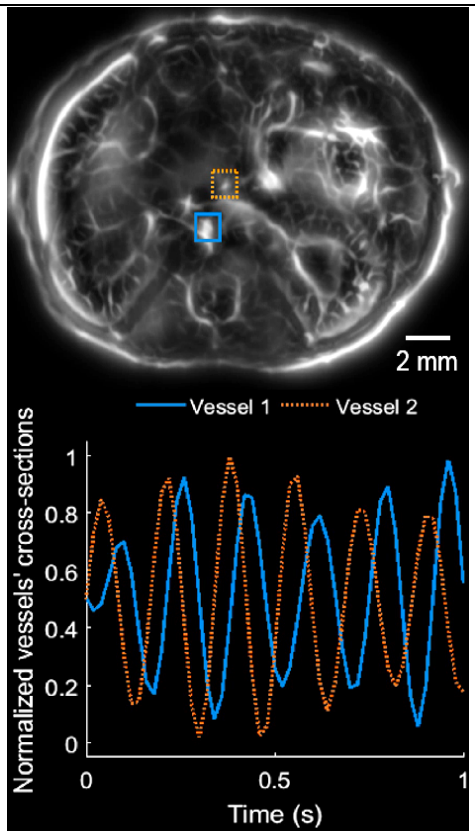	Not demonstrated
Quantifies the pulse wave phase difference between deep arteries		
Visualization of circulating tumor cells *in vivo* over a large field of view	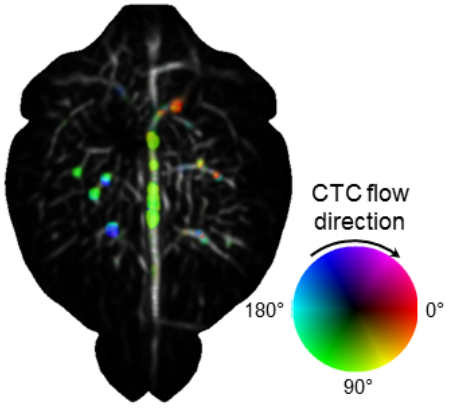	Not demonstrated
Visualizes the movement of melanoma cells within a large field of view (12×10 mm^2) *in vivo*, without labeling and in real time		

Whole-brain imaging of rats *in vivo*	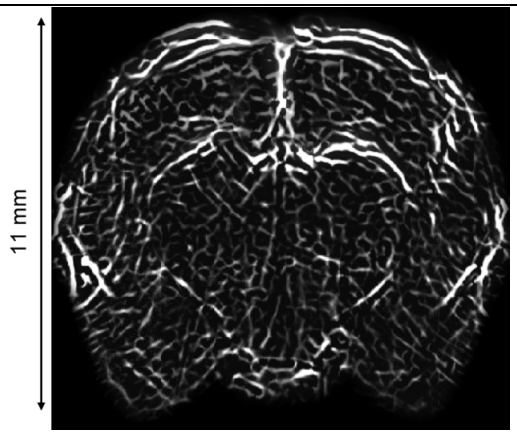 Images throughout an adult rat brain *in vivo* with detailed vasculature revealed	Not demonstrated
Deep brain functional imaging	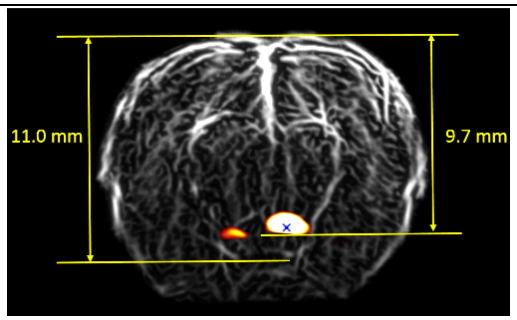 Maps an adult *rat* brain's resting-state functional connectivity as deep as 9.7 mm *in vivo*	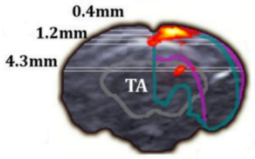 Maps a *mouse* brain's epileptic connectivity (strong response) as deep as only 4.3 mm with low resolution
Maximum demonstrated imaging width *in vivo*	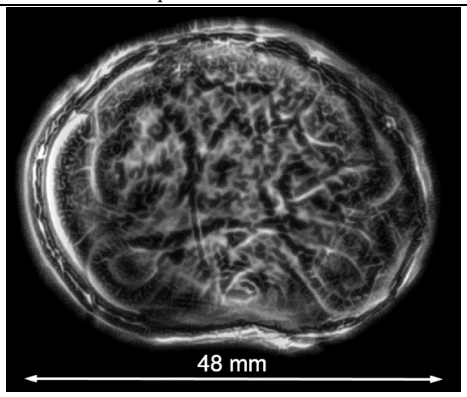 **48 mm**: demonstrated in adult *rats*	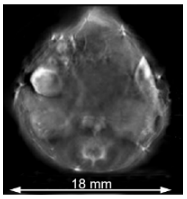 **18 mm**: demonstrated in immature *mice*

Supplementary Figures

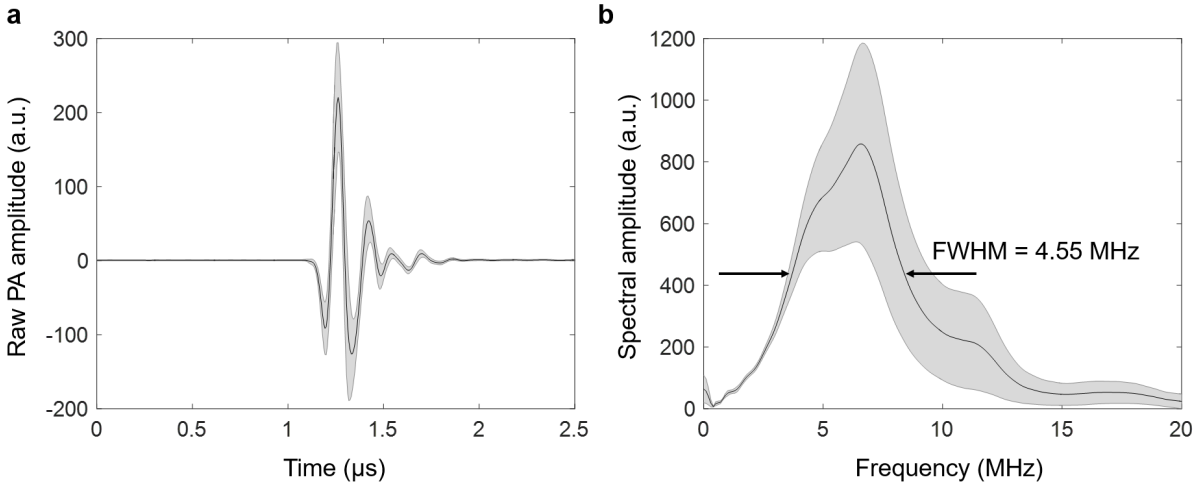

Supplementary Figure 1. The electrical impulse response (EIR) of the SIP-PACT system. (a) The raw radio frequency (RF) signal from each ultrasonic transducer element corresponding to a point PA source at the center of the full-ring array. The black solid line represents the mean value of all transducer elements' responses, and the gray region represents the standard deviation across the elements. (b) Fourier transform amplitude of each RF signal in (a), showing the bandwidth of the transducer array is about 4.55 MHz. The black solid line represents the mean value of the spectral amplitude of all RF signals, and the gray region represents the standard deviation across the elements. The point source was created by depositing red epoxy on a single mode fiber tip. The deposited epoxy, measured about 30 μm × 30 μm × 50 μm, is small enough to be regarded as a spatial point source for the SIP-PACT system. After the fiber tip was positioned in the acoustic focal plane of the transducer array and the center of the full-ring array, a nanosecond excitation pulse was fired through the single mode fiber.

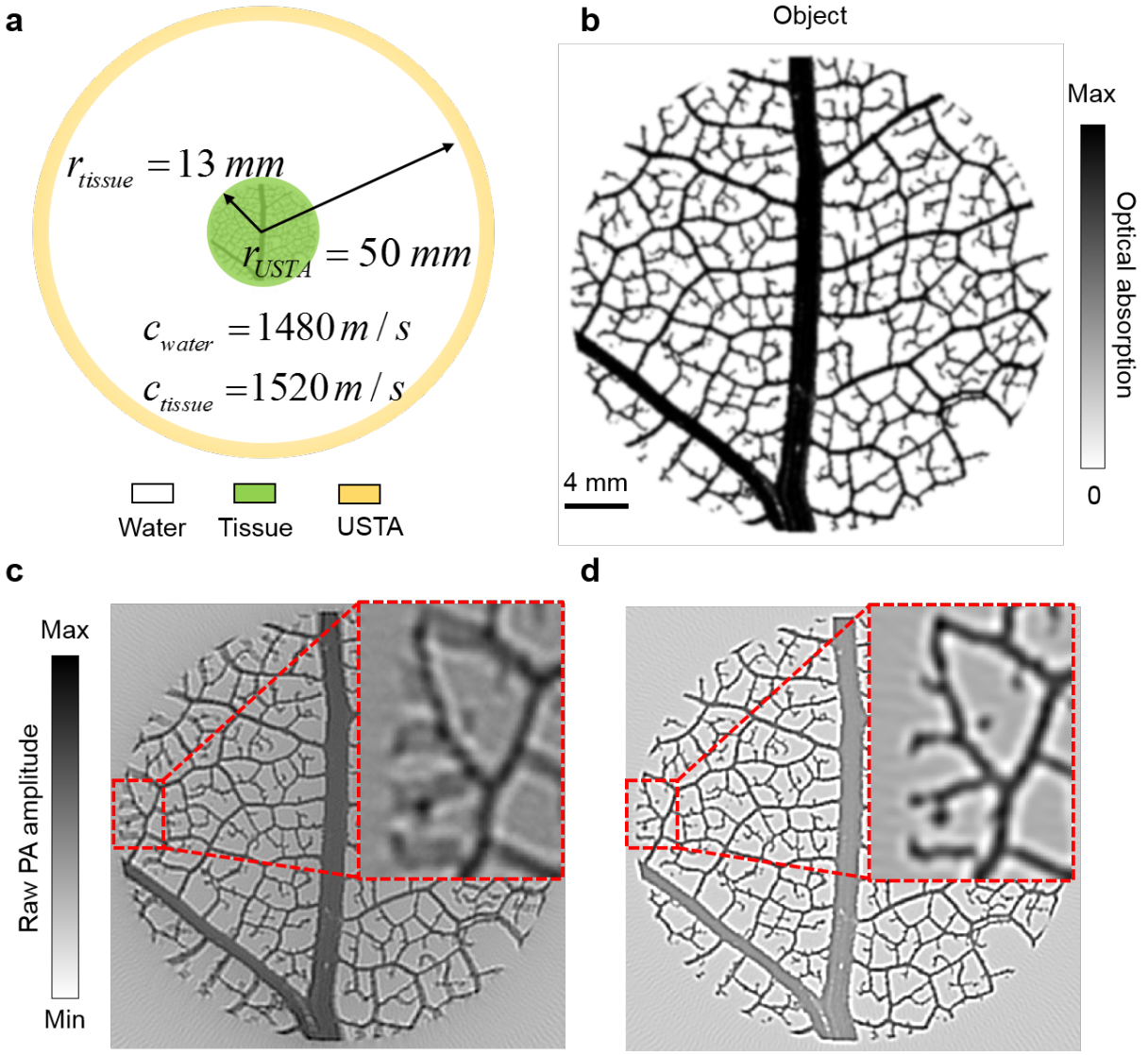

Supplementary Figure 2. Numerical simulation results of dual-speed-of-sound reconstruction, forward data is generated by the k-Wave toolbox (http://www.k-wave.org/). (a) Schematic of the simulation. (b) The optical absorption distribution of the numerical phantom. Reconstructed images using universal back projection based on (c) single speed with v = 1489.8 m/s and (d) dual speed with v_1 = 1480 m/s (in water) and v_2 = 1520 m/s (in tissue), where the close-up insets show the splitting artifacts due to the unmatched speed of sound.

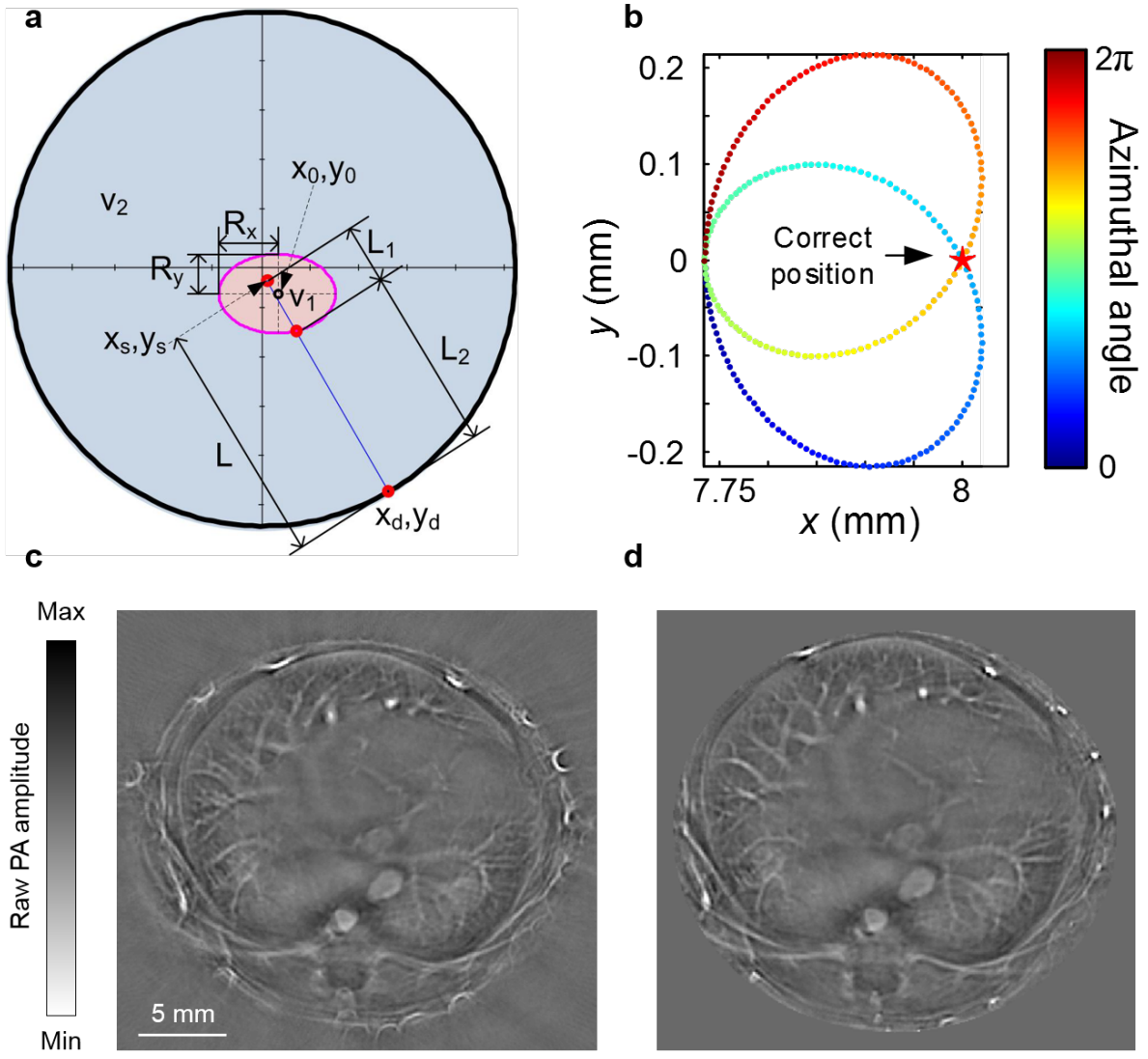

Supplementary Figure 3. Image quality improvement by dual-speed-of-sound reconstruction. (a) Definition of parameters used in half-time dual-speed-of-sound universal back projection. (b) Position of a point source back-projected using single-speed reconstruction. Color represents the in-plane azimuthal angle of the transducer array. In the calculation, $R_x = R_y = 10$ mm, $x_0 = y_0 = 0$, $v_1 = 1.570$ mm/μs (in tissue), $v_2 = 1.506$ mm/μs (in water), and $R_d = 50$ mm. The correct position of the point source is labeled by the red star. (c) and (d) *In vivo* images of a cross-section of a mouse trunk (liver) reconstructed using half-time universal back projection based on (c) single speed with $v = 1.520$ mm/μs and (d) dual speed with $v_1 = 1.590$ mm/μs (in tissue) and $v_2 = 1.507$ mm/μs (in water).

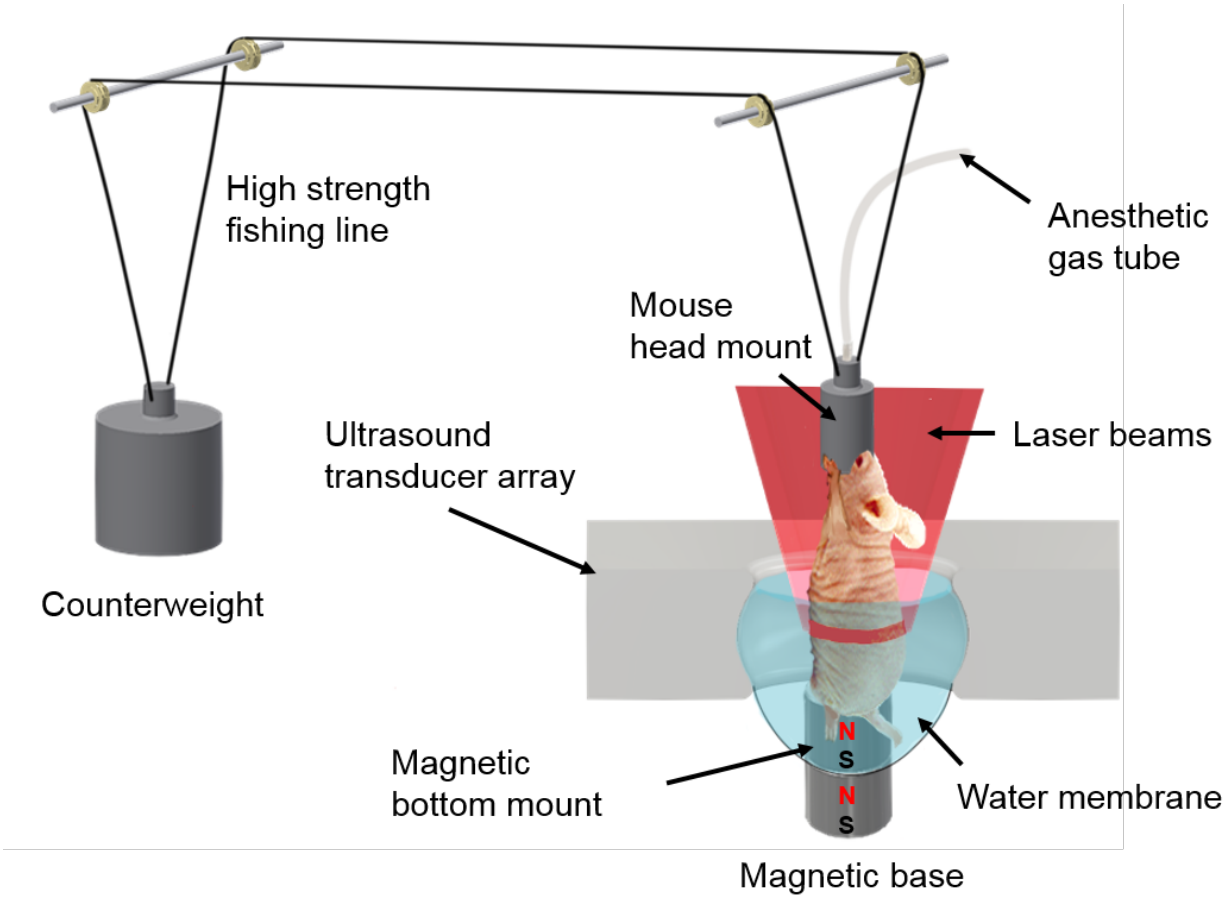

Supplementary Figure 4. Schematic of the animal holder for trunk imaging. The mouse was held upright during imaging. The head and forearms were attached to the head mount, and the hind legs were taped to the magnetic bottom mount. The combination of a magnet and a counterweight keeps the animal straight during vertical scanning.

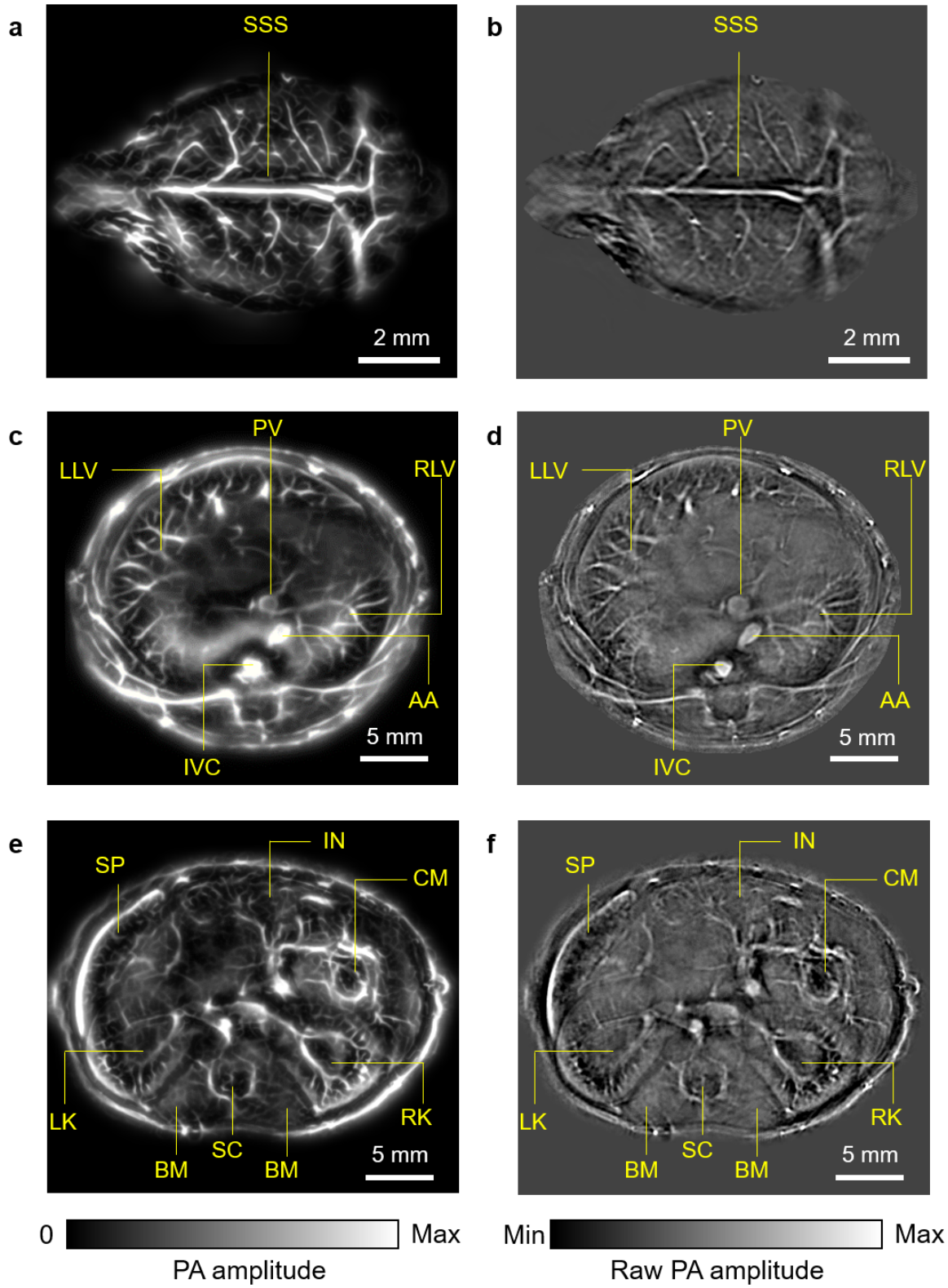

Supplementary Figure 5. Comparison of enhanced images and original reconstructed images using half-time dual-speed-of-sound universal back projection. (a) Enhanced and (b) original images of the mouse cortical vasculature, SSS, superior sagittal sinus. (c) Enhanced and (d)

original cross-sectional images of the two lobes of the liver, AA, abdominal aorta; IVC, inferior vena cava; LLV, left lobe of liver; PV, portal vein; RLV, right lobe of liver. (e) Enhanced and (f) original cross-sectional images of the lower abdominal cavity, BM, backbone muscles; CM, cecum; IN, intestines; LK, left kidney; RK, right kidney SC, spinal cord; SP, spleen.

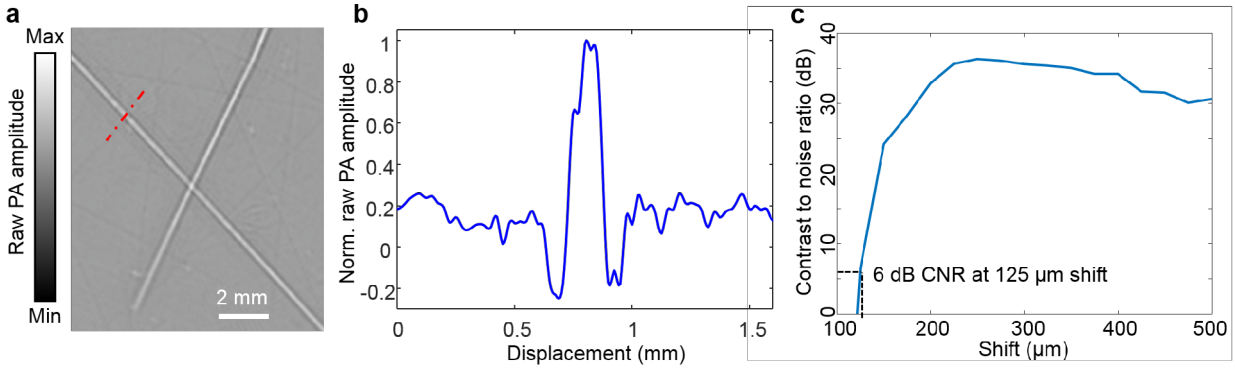

Supplementary Figure 6. Quantification of the in-plane resolution of the SIP-PACT system. (a) An image of two crossed tungsten wires, each with a nominal diameter of 50 μm. (b) The photoacoustic amplitude distribution along the red dash-dot line in (a). (c) The contrast-to-noise ratio (CNR) versus the shift in the sum of the original line profile shown in (b) and the shifted one. The in-plane resolution, defined as the shift corresponding to 6-dB CNR, is 125 μm.

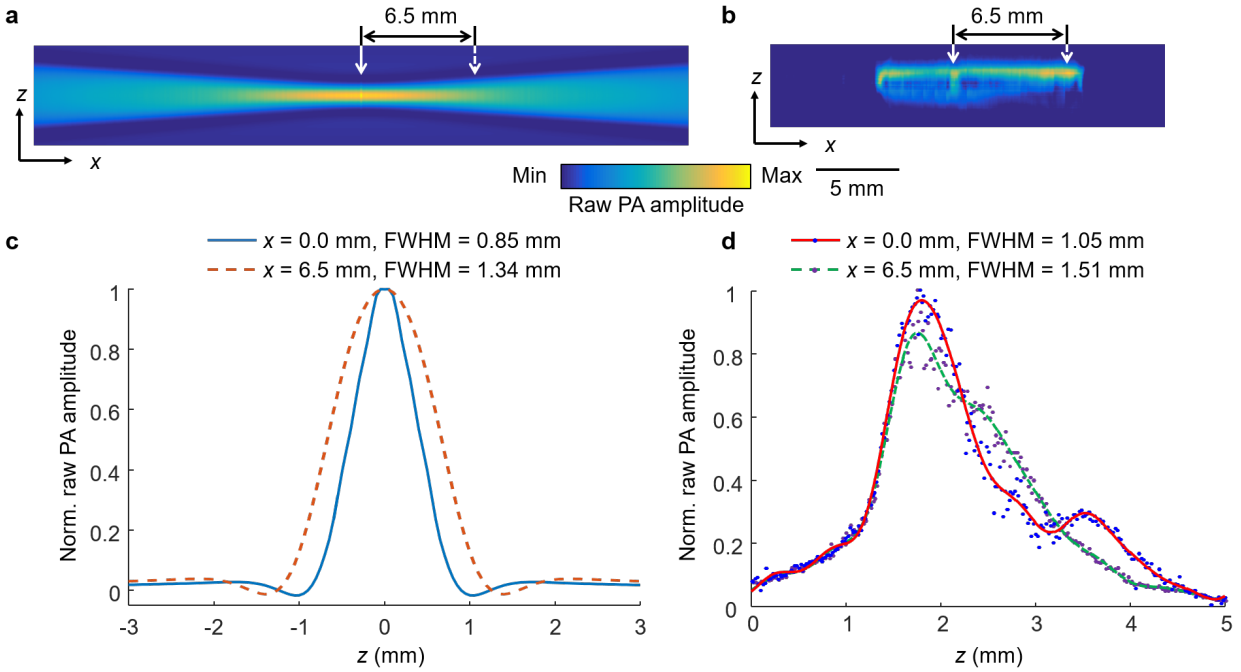

Supplementary Figure 7. Quantification of elevational resolution. (a) Simulated acoustic focus field in the *x*-*z* plane. (b) The photoacoustic image of a tungsten wire with a nominal diameter of 50 µm, projected on the *x*-*z* plane. (c) The simulated line profiles of (a) at the center of the ring (indicated in (a) by the solid white arrow) and at 6.5 mm (off-center, indicated in (a) by the dashed white arrow). (d), as (c), but showing the measured line profiles of (b).

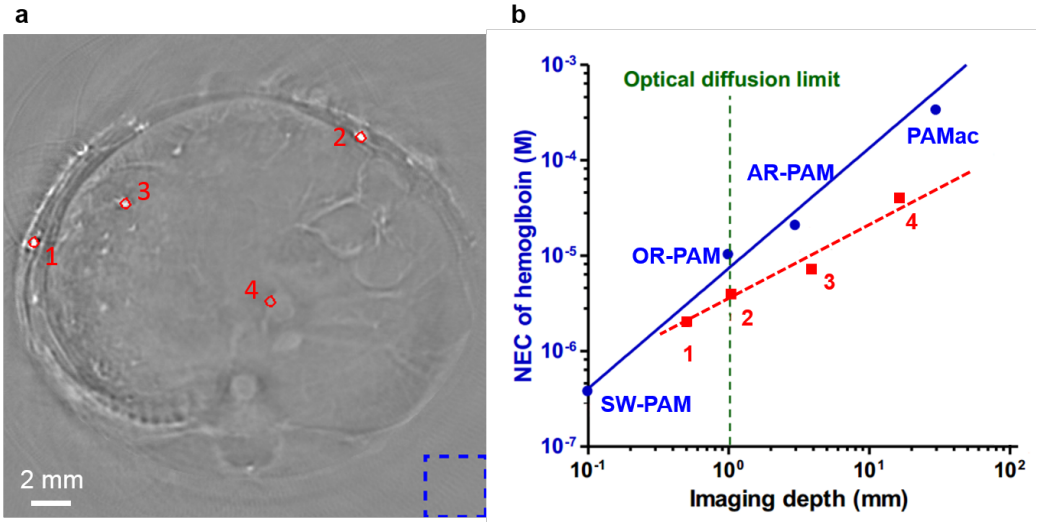

Supplementary Figure 8. Detection sensitivity of SIP-PACT. The noise-equivalent molar concentration (NEC) of hemoglobin was used for the quantification of detection sensitivity[6]. For a fair comparison, the incident fluence of SIP-PACT is scaled to the American National Standards Institute (ANSI) safety limit for the skin at 1064 nm (100 mJ/cm^2 at the skin surface at a 10-Hz repetition rate). (a) A cross-sectional image of the upper abdominal cavity. The red circles label the vessels selected for signal amplitude quantification and the blue dashed square labels the region selected for noise level quantification. And the NEC is calculated using the same method reported in the literature[6]. (b) Comparison of detection sensitivity of SIP-PACT and the reported values in the literature[6]. The blue dots are the values reported in the literature and the blue solid line is the fit; the red squares are the NEC of SIP-PACT quantified from the vessels in (a) and the red dashed line is the fit.

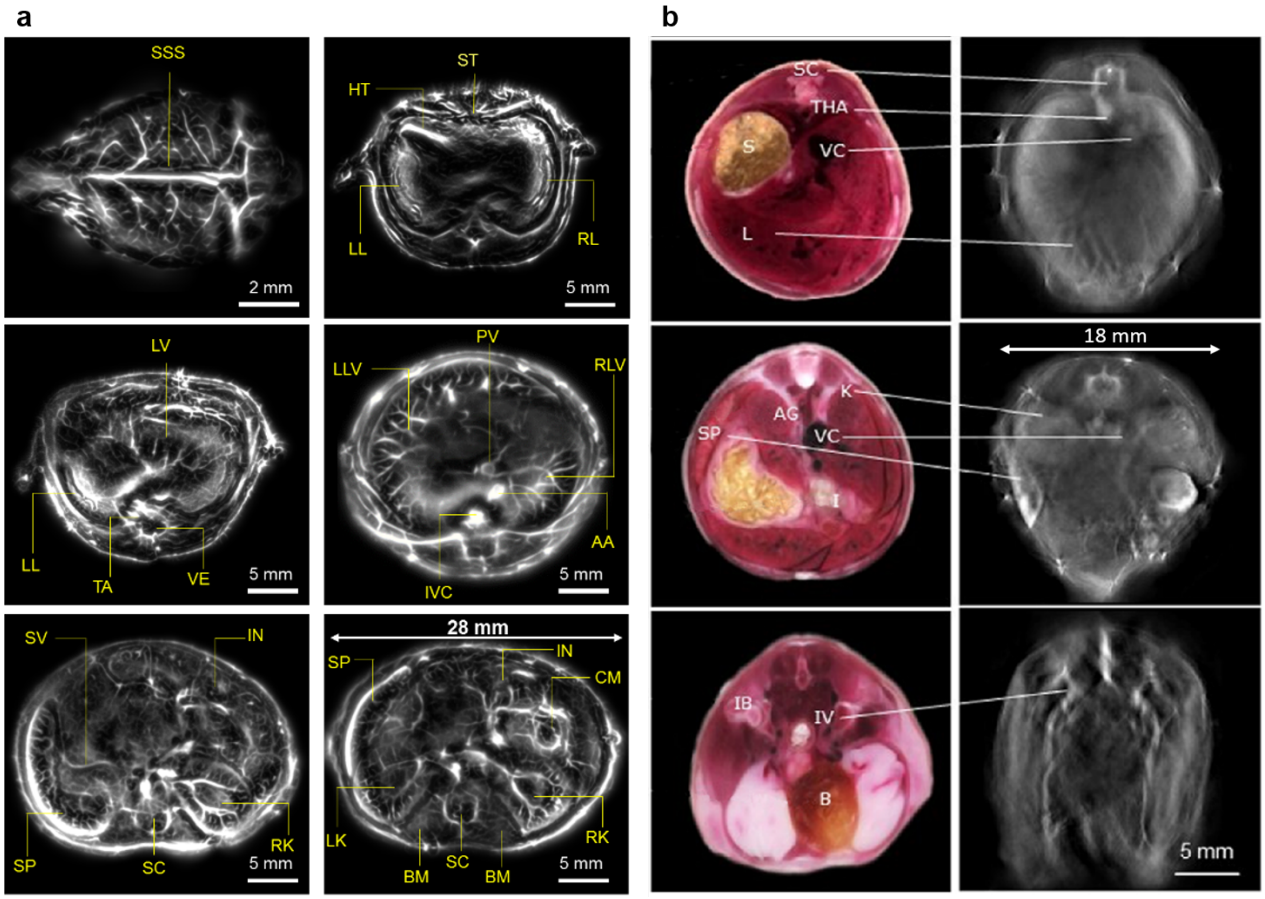

Supplementary Figure 9. Comparison of whole-body images from SIP-PACT and state-of-the-art small animal PACT[1]. (a) Cross-sectional images of mouse whole-body anatomy, from brain to lower abdominal cavity, acquired by SIP-PACT. (b) Right column: cross-sectional images acquired by the state-of-the-art PACT[1], commercially available from iThera Medical GmbH. Left column: reference macroscopic RGB pictures of cross sections of the frozen mouse taken from approximately the same area as the right column. Annotations for (a): AA, abdominal aorta; BM, backbone muscles; CM, cecum; HT, heart; IN, intestines; IVC, inferior vena cava; LK, left kidney; LL, left lung; LLV, left lobe of liver; LV, liver; PV, portal vein; RK, right kidney; RL, right lung; RLV, right lobe of liver; SC, spinal cord; SP, spleen; SSS, superior sagittal sinus; ST, sternum; SV, splenic vein; TA, thoracic aorta; VE, vertebra. Annotations for (b): AG, adrenal gland; B, bladder; I, intestines; IB, iliac body; IV, iliac vein; K, kidney; L, liver; P, pancreas; S, stomach; SC, spinal cord; SP, spleen; THA, thoracic aorta; VC, vena cava. The SIP-PACT images show detailed structures and vasculatures of internal organs, while state-of-the-art PACT images barely differentiate the internal organs due to the low contrast. The image quality of SIP-PACT is much higher than that of the state-of-the-art PACT.

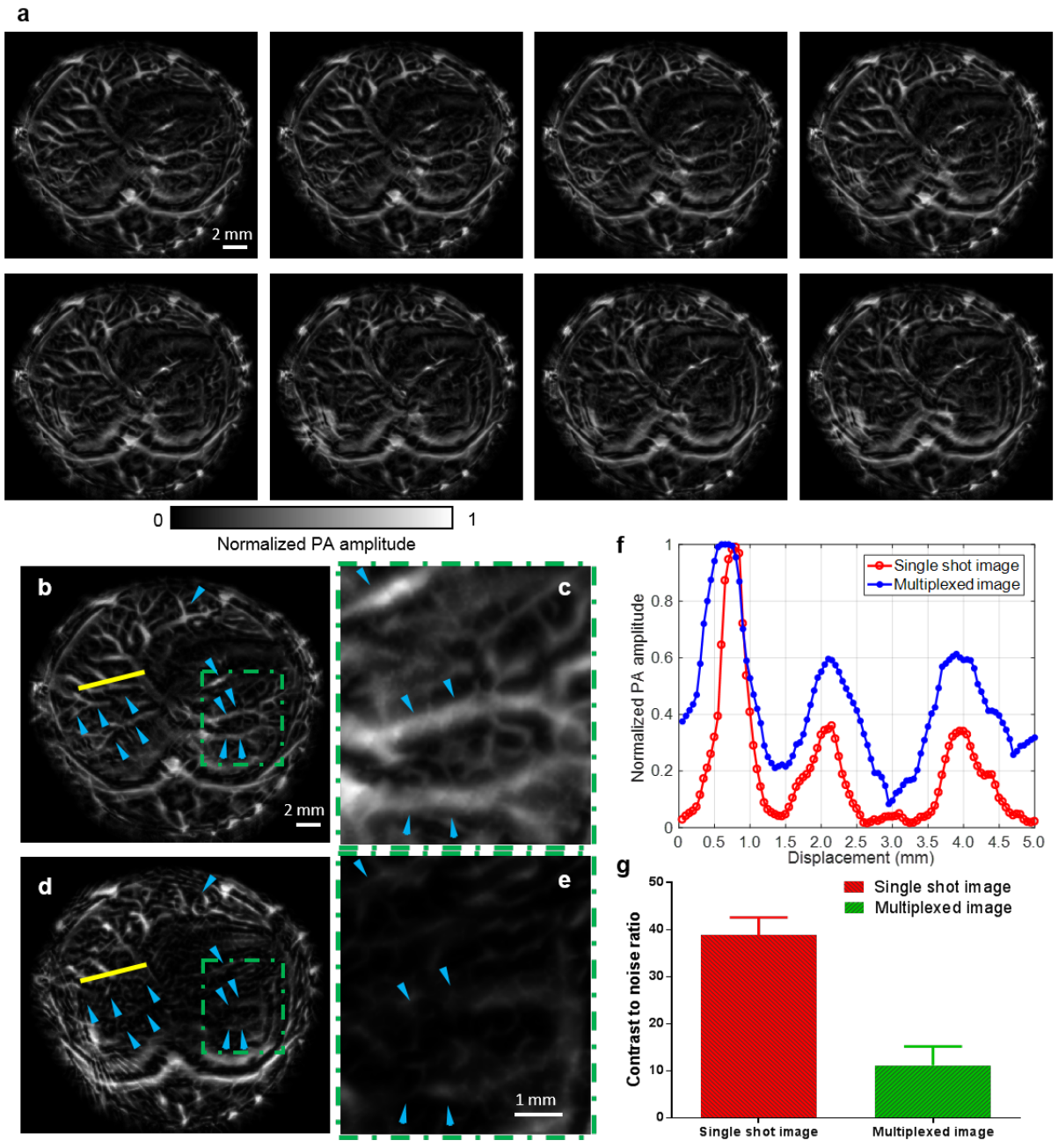

Supplementary Figure 10. Effect of multiplexing on imaging quality. (a) Eight consecutive images acquired by SIP-PACT, shown left to right in two rows. (b) The first image of (a). (c) Close-up image of the green dashed box in (b). (d) Image simulated with 8-to-1 multiplexing from the raw data for the images in (a). (e) Close-up image of the green dashed box in (d). Cyan arrows point out the features present in (b) and (c) but missing (d) and (e). (f) Profiles of the yellow lines in (b) and (d), which clearly show that multiplexing blurs the vessels and degrades the image resolution. (g) The contrast-to-noise ratios of the images in (c) and (e), which show that multiplexing decreases the image contrast.

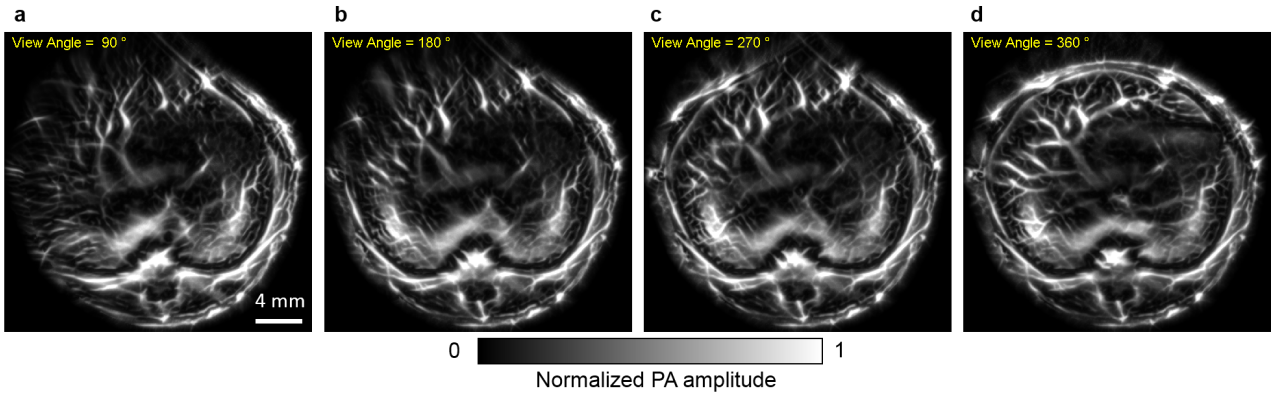

Supplementary Figure 11. Effect of the detection view angle on image quality. (a to d) Reconstructed images with detection view angles ranging from 90 degrees to 360 degrees, which show that more structures are discernable with fewer reconstruction artifacts as the view angle increases. With a 360-degree (full-view) view angle, the reconstructed image has the best image quality and least streaking artifacts. The images are reconstructed using the half-time dual-speed-of-sound universal back-projection method.

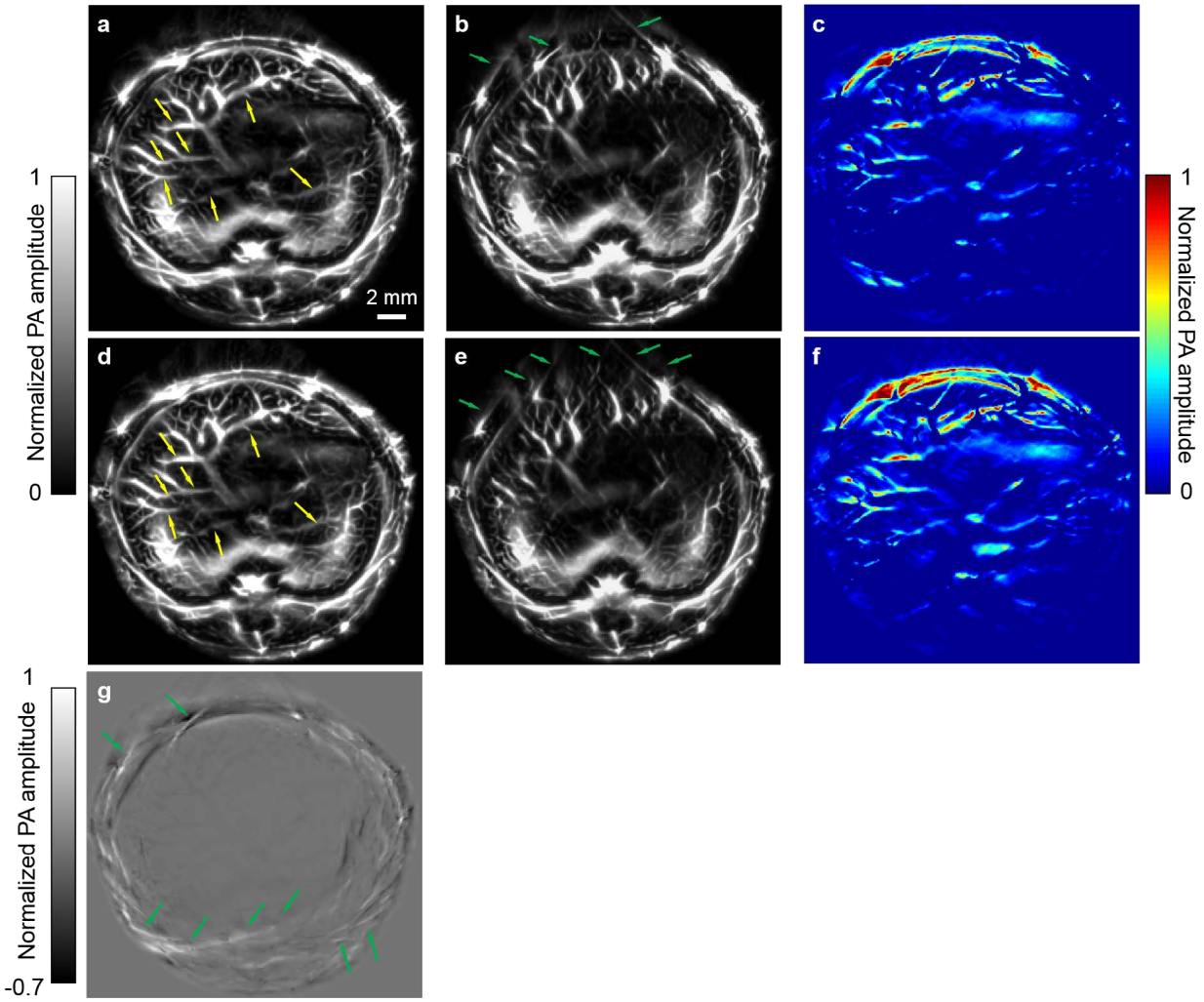

Supplementary Figure 12. Comparison of images reconstructed using full- and half-time algorithms with view angles of 270 and 360 degrees. (a) Image with 360-degree detection view angle, reconstructed using the full-time dual-speed-of-sound universal back-projection method. (b) Image with 270-degree detection view angle, reconstructed using the full-time dual-speed-of-sound universal back-projection method. The yellow arrows in (a) point out the missing features in the limited view angle image, while the green arrows in (b) point out reconstruction artifacts induced by the limited view angle. (c) Differential image between (a) and (b). A threshold of 0 was applied and only the positive values are shown, which illustrates the features in (a) that are missing in (b). (d) Image with 360-degree detection view angle, reconstructed using the half-time dual-speed-of-sound back-projection method. (e) Images with 270-degree detection view angle, reconstructed using the half-time dual-speed-of-sound universal back-projection method. The yellow arrows in (d) point out the missing features in the limited view angle image, while the green arrows in (e) point out the reconstruction artifacts induced by the limited view angle. (f) Differential image between (d) and (e). A threshold of 0 was applied and only the positive values are shown, which illustrates the features in (a) that are missing in (b). (g) A differential image between (a) and (d), which shows that half-time reconstruction minimizes the reconstruction artifacts induced by PA signals reflected multiple times by the bones inside the animal. Thus, the

combination of a full-view detection and half-time dual-speed-of-sound universal back-projection reconstruction provides the best image quality.

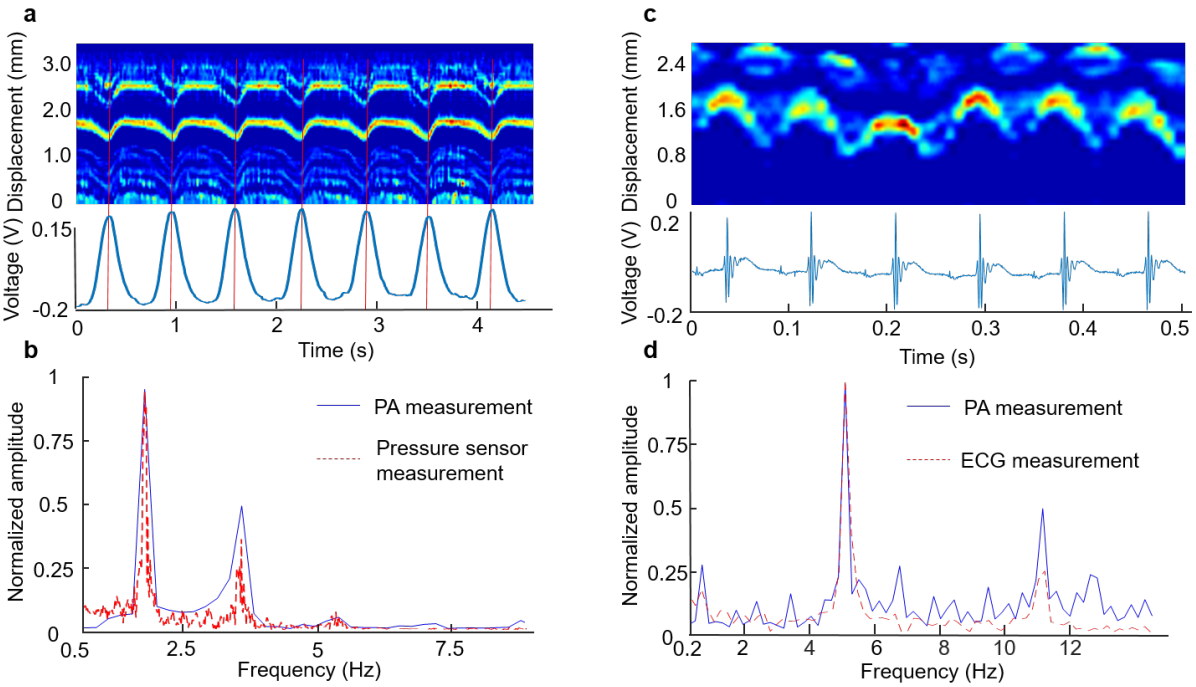

Supplementary Figure 13. Validation of the SIP-PACT measurement of breathing motion and heartbeats. The pressure sensor and electrocardiography (ECG) measurement were conducted in parallel with the SIP-PACT imaging on the same mouse. (a) Co-registered measurement of breathing motion from SIP-PACT (top) and the pressure sensor (bottom). (b) Fourier transform of (a), which shows the identical respiratory frequency measured by SIP-PACT and the pressure sensor. (c) Co-registered measurement of heartbeats from SIP-PACT (top) and ECG (bottom). (d) Fourier transform of (b), which shows the identical heartbeat frequency measured by SIP-PACT and ECG.

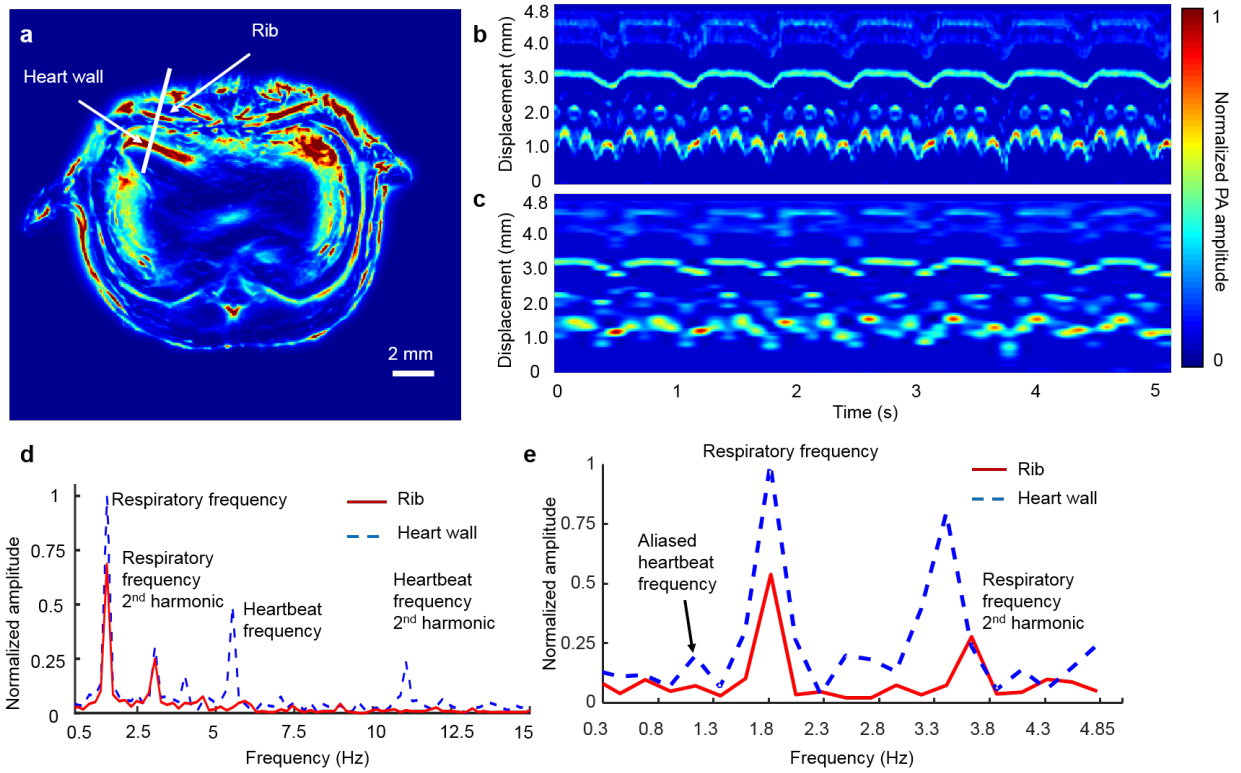

Supplementary Figure 14. Comparison of images with frame rates of 50 Hz and 10 Hz. (a) Cross-sectional image of the upper thoracic cavity, where the white solid line crosses a rib and the heart wall. (b) A 50-Hz frame rate line profiles in (a) versus time, showing the displacements of the rib during respiration and the heart wall during heartbeats. (c) A 10-Hz frame rate line profiles in (a) versus time, showing the displacements of the rib during respiration and the heart wall during heartbeats. (d) Fourier transforms of the rib and heart wall movements in (b) showing the respiratory frequency and heartbeat frequency, respectively. (e) Fourier transforms of the rib and heart wall movements in (c) showing the respiratory frequency, but with the heartbeat frequency aliased due to the low frame rate. An inaccurate physiological measurement could result from using 10-Hz frame rate.

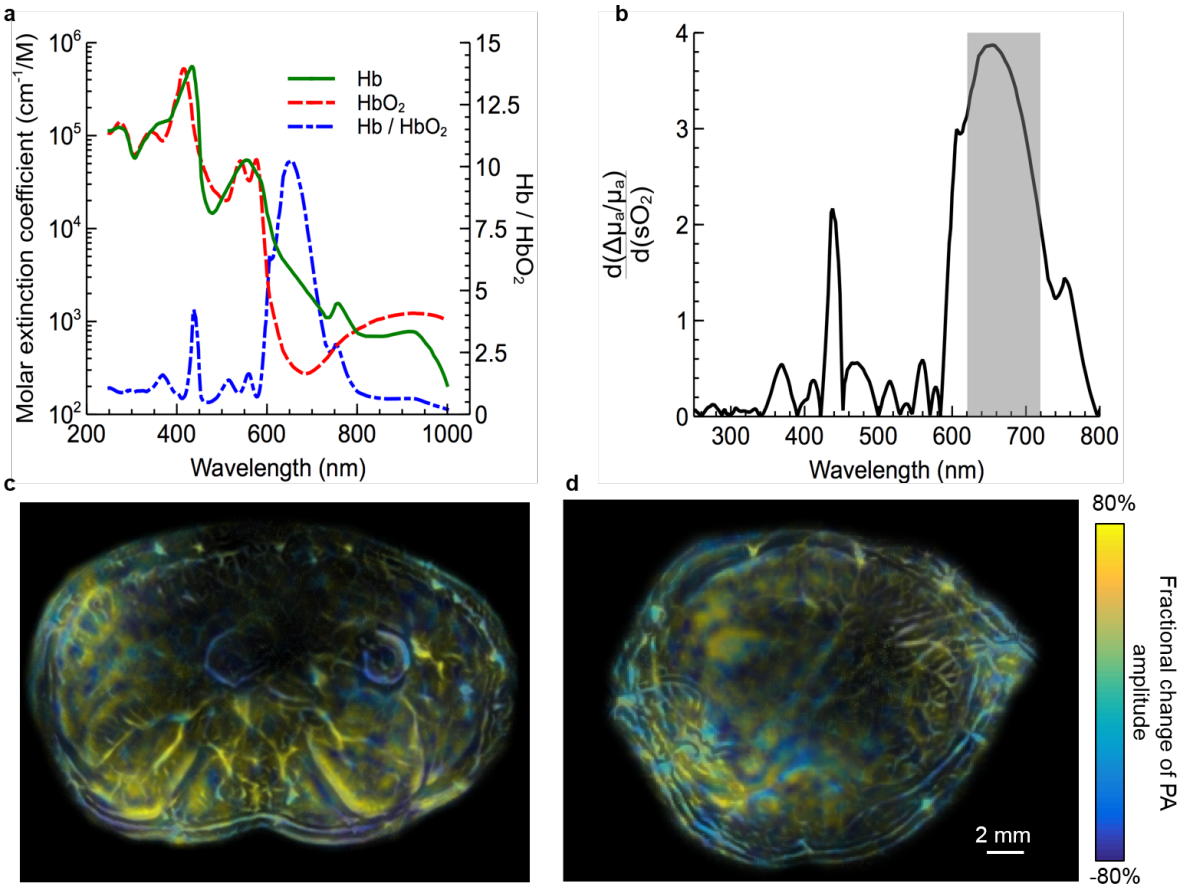

Supplementary Figure 15. (a) The absorption spectra of oxy-hemoglobin (HbO_2) and deoxy-hemoglobin (Hb), and the absorption ratio of deoxy-hemoglobin to oxy-hemoglobin (Hb/HbO_2). (b) Fractional changes of blood's absorption coefficient (μ_a) corresponding to the blood sO_2 change ($d(\Delta\mu_a/\mu_a) / d(sO_2)$) with visible and NIR light illumination. Wavelengths from 626 nm to 720 nm provide an sO_2 sensitive imaging window for SIP-PACT (highlighted by the gray area). (c) Fractional changes of blood oxygen levels in the cross-section of the lower abdominal cavity during oxygen challenge. (d) Fractional changes of blood oxygen levels in the cross-section of the two lobes of the liver during oxygen challenge.

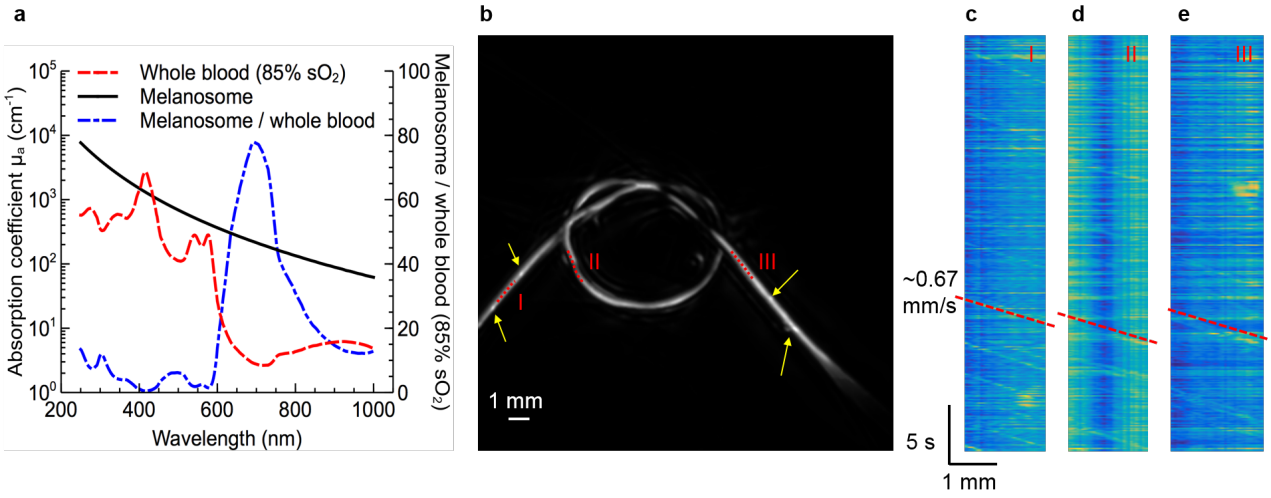

Supplementary Figure 16. (a) Spectra of whole blood (85% sO_2) and melanosome, and the absorption ratio of melanosome and whole blood, which peaks at 680 nm. The melanosome to blood contrast can be maximized with 680-nm excitation. (b) Image of a tube (300 μm in diameter) filled with the mixture of blood and melanoma cells (10^6 cells in 2 mL of bovine blood). The mixture of blood and melanoma cells is driven by a syringe to flow through the tube. The melanoma cells (or cluster) are highlighted by the yellow arrows. (c–e) Time trace plot of each pixel along the red dashed line in (b). The space-time domain slope in (c–e) were computed by linear fitting as ~0.67 mm/s, representing the flow speed of melanoma cells.

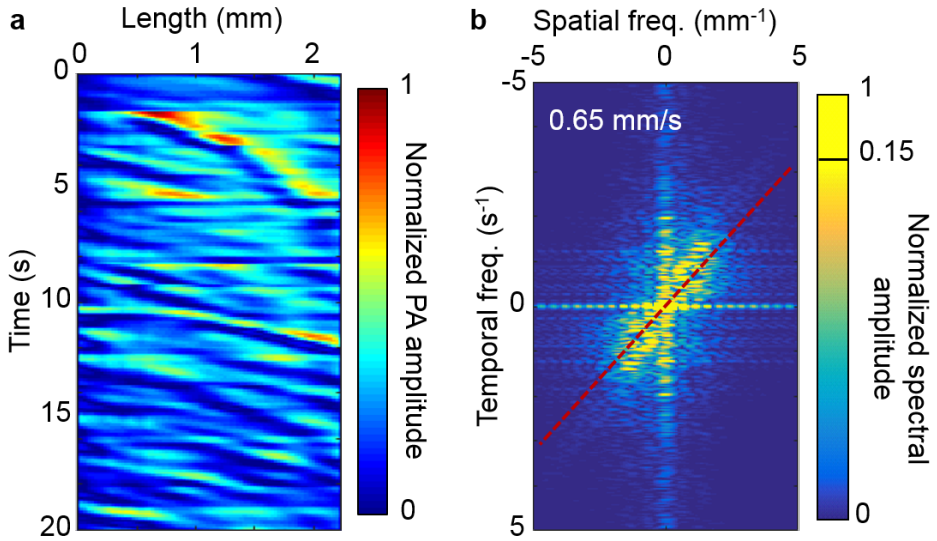

Supplementary Figure 17. (a) Time trace plot of each pixel along the red dashed line in Fig. 5a. (c) 2D Fourier transform of (a), which maps lines with the same slope in the space-time domain onto a single line in the spatiotemporal frequency domain. The slope of the red dashed line, computed by linear fitting as 0.65 mm/s, represents the flow speed of CTCs. The spectral amplitude values were normalized according to the maximum value, and were saturated at 0.15 for display purposes.

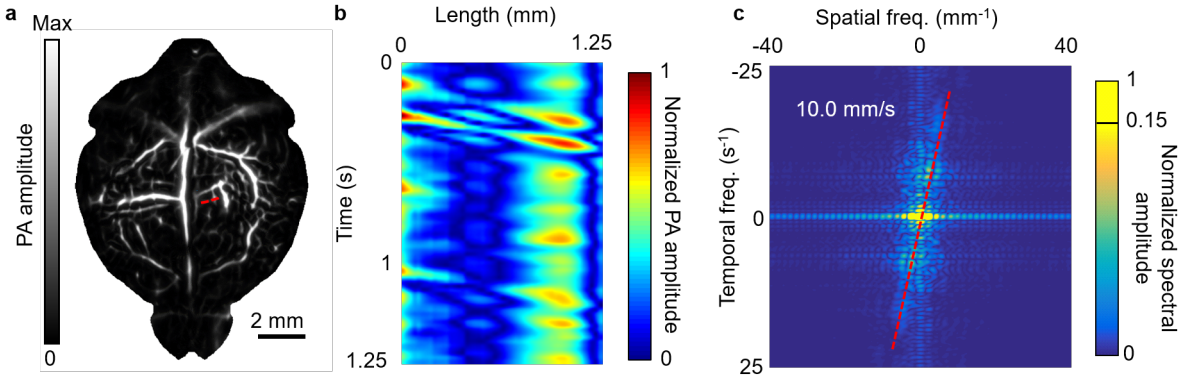

Supplementary Figure 18. (a) PA image of the mouse brain cortex after injection of melanoma cancer cells. (b) The time trace plot of each pixel along an artery (the red dashed line in (a)). (c) 2D Fourier transform of (b), which maps lines with the same slope in the space-time domain onto a single line in the spatiotemporal frequency domain. The slope of the red dashed line, computed by linear fitting as 10.0 mm/s, represents the flow speed of CTCs, which is higher than that in veins.

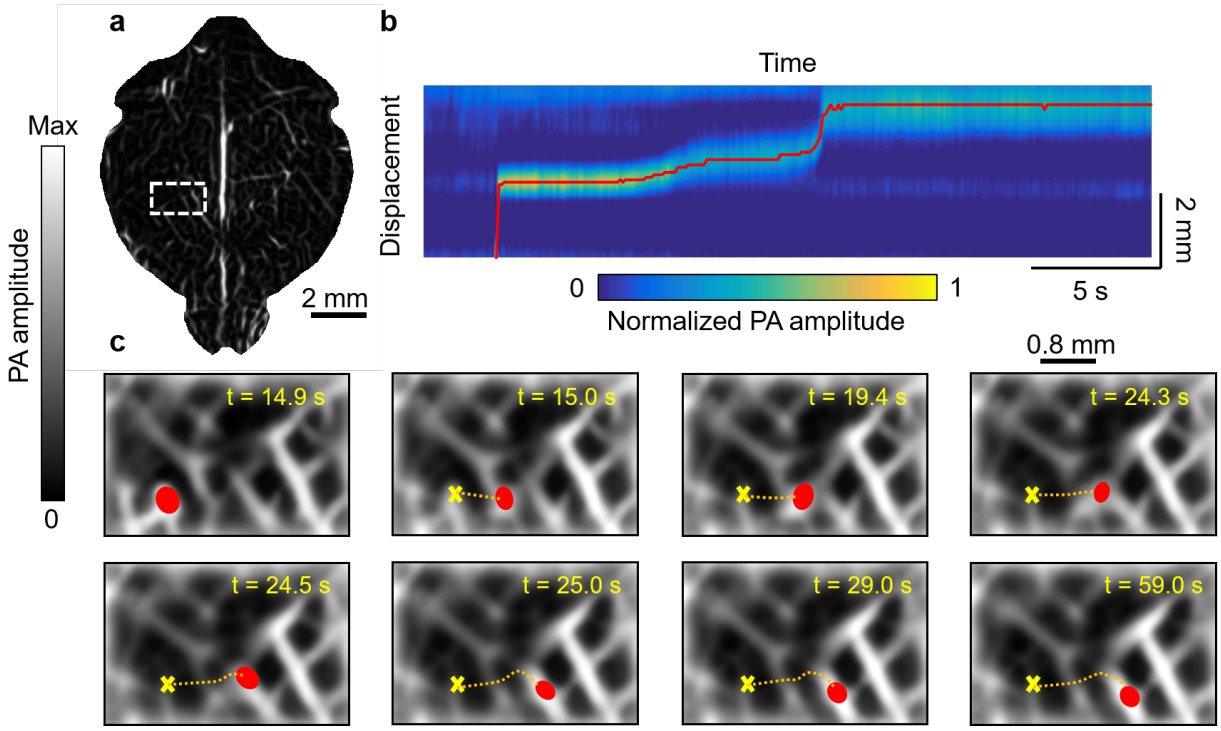

Supplementary Figure 19. *In vivo* observation of CTCs whose motion in mouse cortex has ceased. (a) The PA image of the mouse brain cortex after injection of melanoma cancer cells. (b) Displacement versus time trace plot of the finally ceased CTCs, where the red line is the displacement of the center position of the non-moving CTCs, and the plateau of the red line represents where and when the CTCs ceased moving. (c) Zoomed-in images of the white dashed box in (a), where the yellow crosses represent the initial center position of the tracked CTC, the red patches label its central position in the current frames, and the orange dashed lines represent the CTCs' flowing traces.

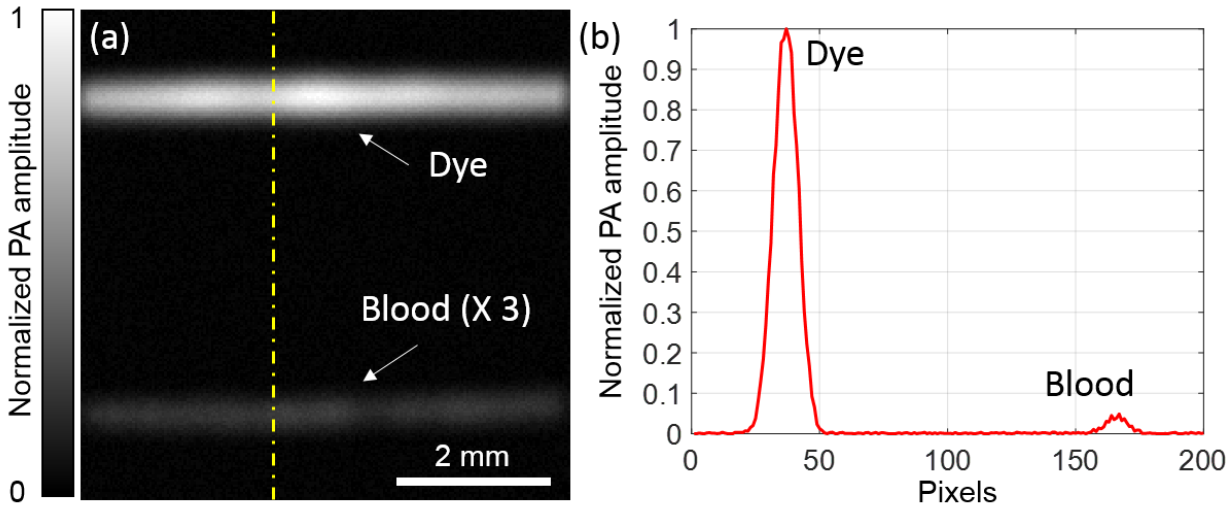

Supplementary Figure 20. Comparison of absorption of dye and bovine blood (90% sO_2) at 1064 nm. The NIR dye (FHI 104422P, Fabricolor Holding Int'l LLC, 0.5% mass concentration in deionized water) and bovine blood are filled in silicone tubes (600 μm diameter), which is embedded in agar. (a) PA image of the two tubes filled with NIR dye and bovine blood, with 1064-nm illumination. The signals from blood are amplified by 3-fold for improved display. (b) Line profile of the yellow dashed line in (a), showing that the NIR dye has 19.8-fold more absorption than blood at 1064 nm. Thus the absorption coefficient of the dye solution is 74.7 cm^{-1}.

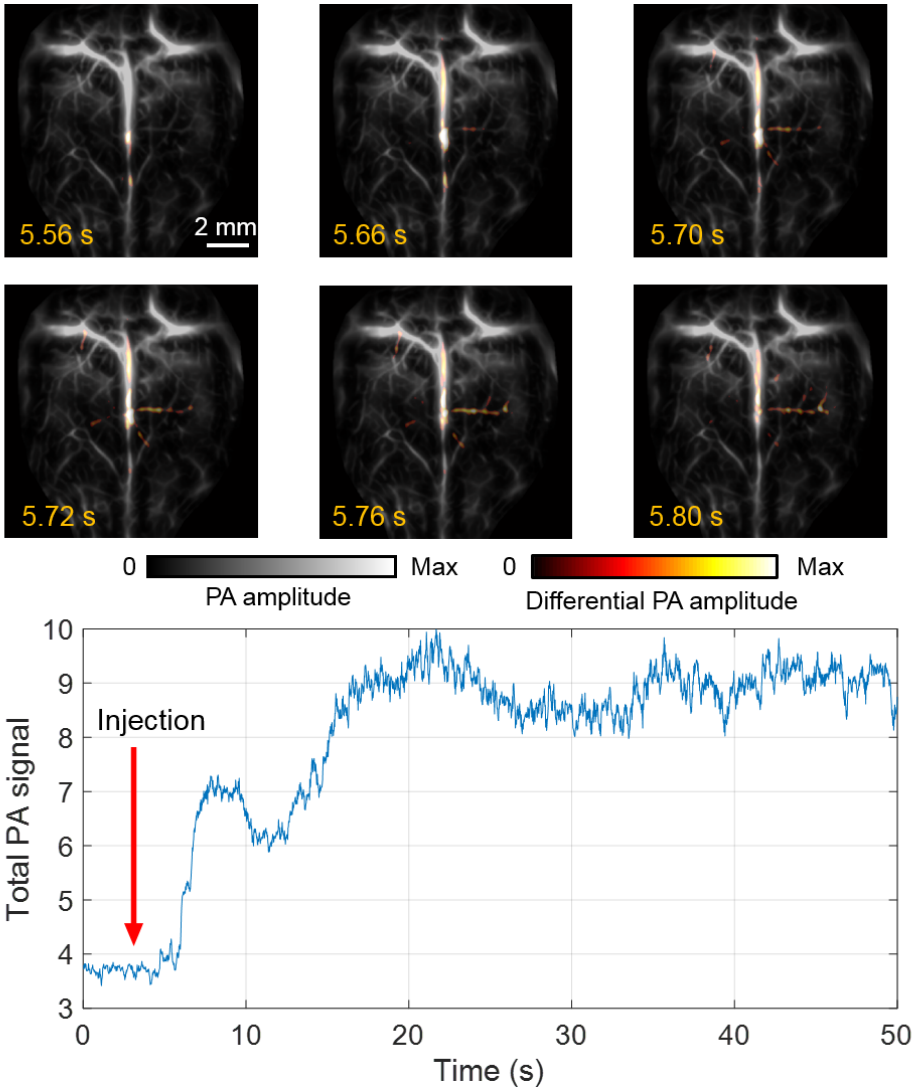

Supplementary Figure 21. Visualization of dye perfusion in the mouse brain. (a) Images of the mouse cortex after the injection of dye solution at different times. (b) The total PA signal of the mouse brain greatly increases after the injection of dye solution.

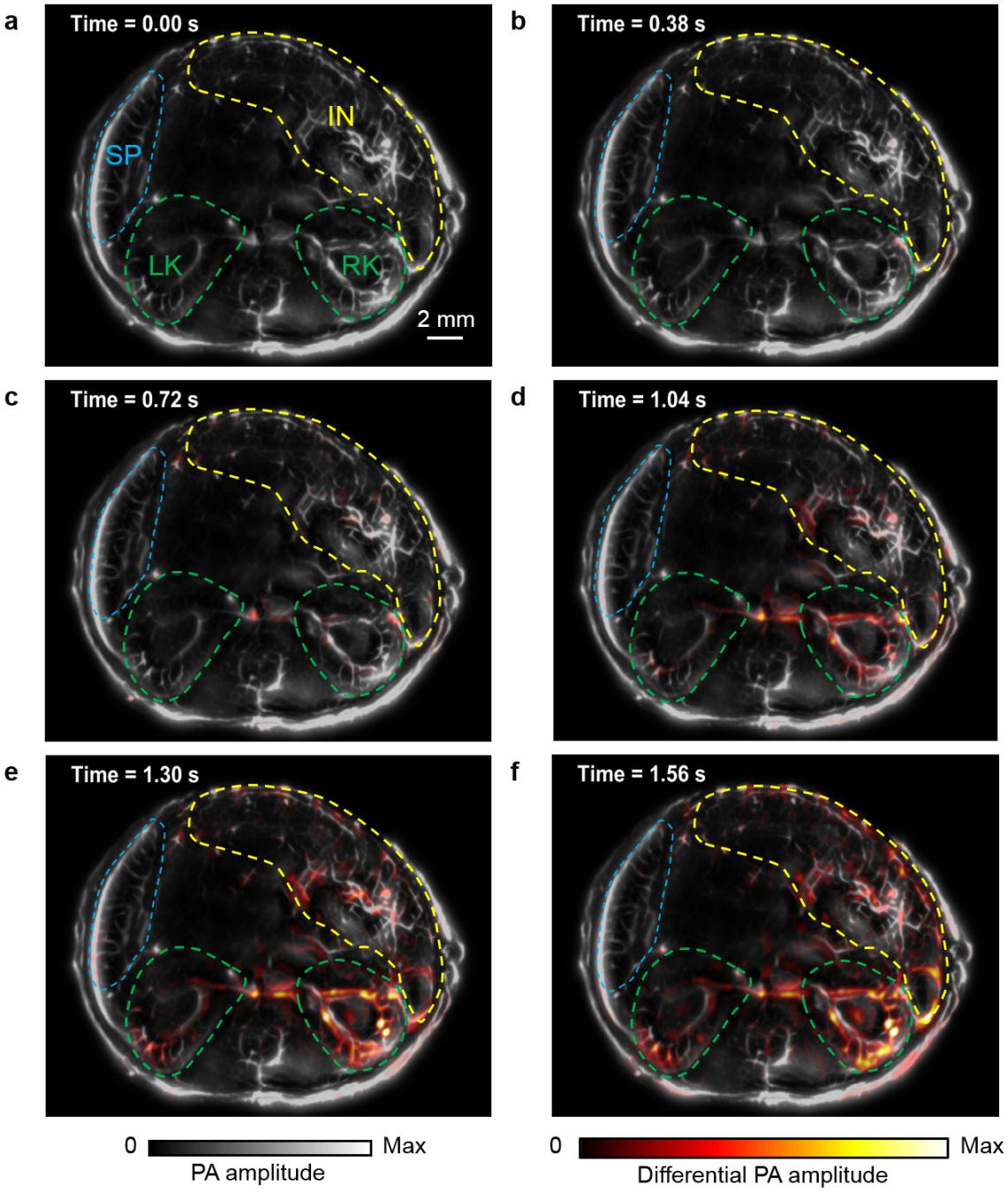

Supplementary Figure 22. Visualization of whole-body dye perfusion. (a–f) Cross-sectional images of the lower abdominal cavity at different times after injection of dye solution, showing that dye molecules perfused to both kidneys and the intestinal region. IN, intestine; LK, left kidney; RK, right kidney; SP, spleen.

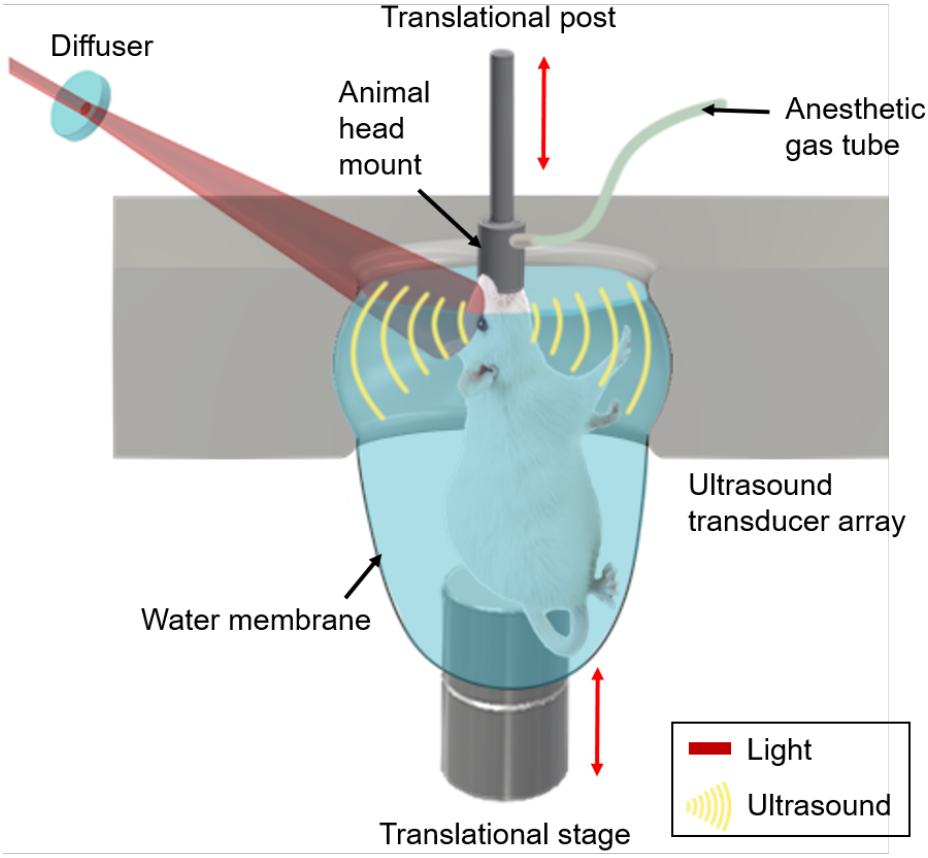

Supplementary Figure 23. Setup of the rat brain imaging. The rat head was mounted vertically during imaging and the light was obliquely delivered to the rat cortex.

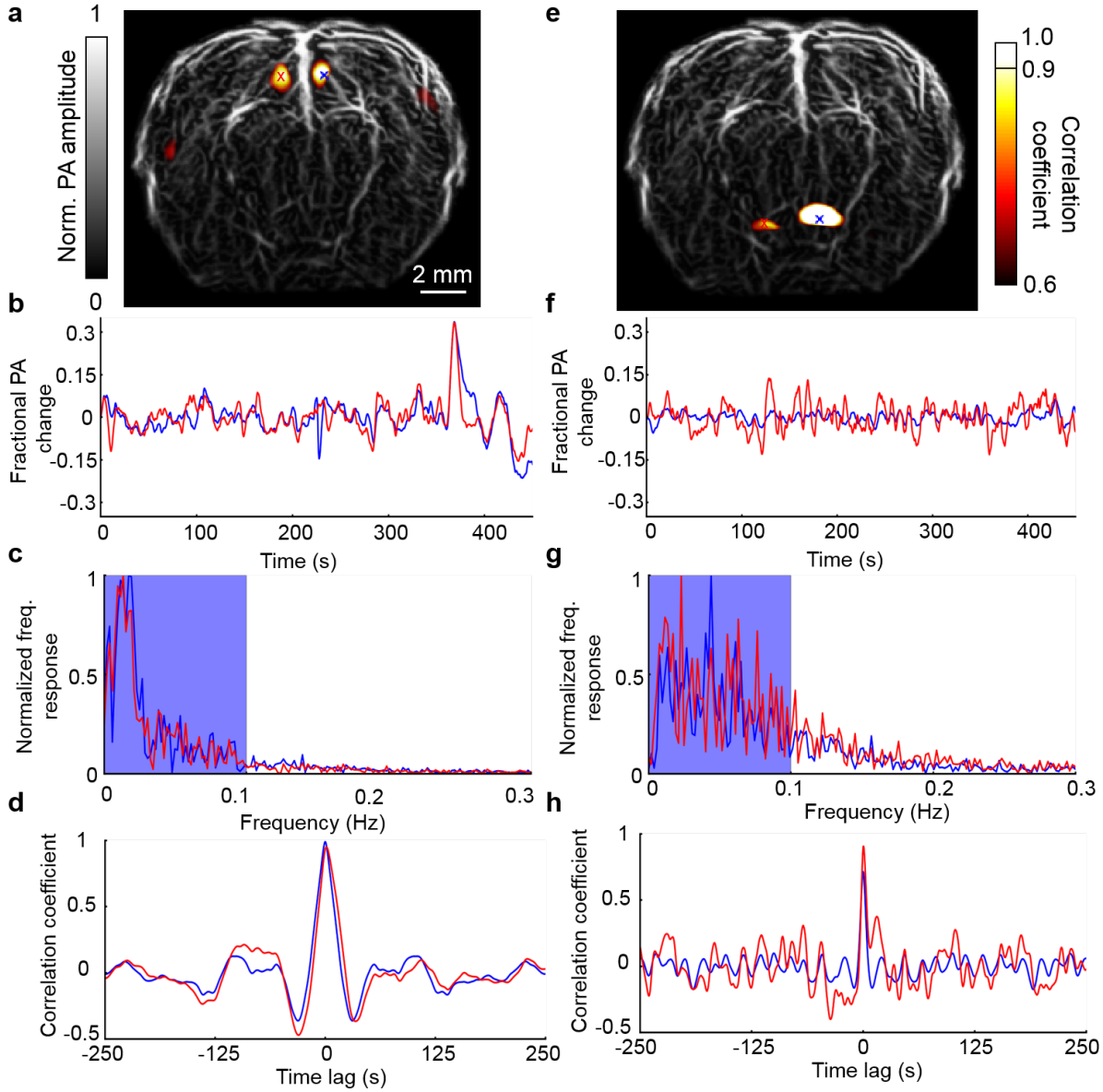

Supplementary Figure 24. Spontaneous hemodynamic variations show high temporal correlation in contralateral regions in a rat brain. (a) Correlation map of the rat brain with a right seed marked by a blue cross. (b) Spontaneous variations in the PA signal in the contralateral regions marked by the blue cross (blue curve) and red cross (red curve) in (a) show high temporal correlations. (c) Frequency distribution of the PA signals in the correlated regions in (a). (d) Temporal correlation function between the signals obtained at the seed region (blue cross spot in (a)) and the nearby region (blue curve, corresponding to the high-intensity spot on the right brain in (a)) or between the same seed region and the contralateral region (red curve, corresponding to the high-intensity spot on the left brain in (a)). (e–h) Similar to (a–d), another set of correlation regions in the deep brain and their temporal hemodynamic responses.

Supplementary Videos

Supplementary Video 1. *In vivo* label-free photoacoustic computed tomography of mouse internal organs. On the bottom-left panel, the red line shows the corresponding elevational position of the cross-sectional images (right panel). The red box on the right panel indicates the position of the close-up images, displayed on the top-left corner. The light fluence on the animal skin was 18 mJ/cm^2 at 1064 nm, with a pulse repetition rate of 50 Hz. Stepping along the animal trunk with a step size of 0.08 mm, a total of 600 cross-sectional images were acquired, with a 25 mm by 30 mm cm field of view.

Supplementary Video 2. *In vivo* label-free photoacoustic computed tomography of mouse whole-body anatomy at a cross-section of the upper thoracic cavity, with contrast enhancement filtering described in Online Methods. The light fluence on the animal skin was 18 mJ/cm^2 at 1064 nm, with a pulse repetition rate of 50 Hz.

Supplementary Video 3. *In vivo* label-free photoacoustic computed tomography of mouse whole-body anatomy at a cross-section of the lower thoracic cavity, with contrast enhancement filtering described in Online Methods. The light fluence on the animal skin was 18 mJ/cm^2 at 1064 nm, with a pulse repetition rate of 50 Hz.

Supplementary Video 4. *In vivo* label-free photoacoustic computed tomography of mouse whole-body anatomy at a cross-section of the liver, with contrast enhancement filtering described in Online Methods. The light fluence on the animal skin was 18 mJ/cm^2 at 1064 nm, with a pulse repetition rate of 50 Hz.

Supplementary Video 5. *In vivo* label-free photoacoustic computed tomography of mouse whole-body anatomy at a cross-section of the upper abdominal cavity, with contrast enhancement filtering described in Online Methods. The light fluence on the animal skin was 18 mJ/cm^2 at 1064 nm, with a pulse repetition rate of 50 Hz.

Supplementary Video 6. *In vivo* label-free photoacoustic computed tomography of mouse whole-body anatomy at a cross-section of the lower abdominal cavity, with contrast enhancement filtering described in Online Methods. The light fluence on the animal skin was 18 mJ/cm^2 at 1064 nm, with a pulse repetition rate of 50 Hz.

Supplementary Movie 7. *In vivo* mouse liver cross-sectional images reconstructed from increasing angular coverage. Angle was gradually increased from 45° to 360°. Reconstruction artifacts are significantly mitigated while angular coverage increases.

Supplementary Video 8. Pulse wave induced cross-sectional area changes of two vertical arteries over time. The right panel co-plots the normalized cross-sectional areas of the two arteries and shows the relatively stable phase delay between them.

Supplementary Video 9. *In vivo* label-free photoacoustic computed tomography of mouse brain response to oxygen challenge. The upper panels show *in vivo* movies of the fractional concentrations of oxy- (HbO_2) and deoxy- (Hb) hemoglobin, as well as the absolute value of oxygen saturation (sO_2) in color. The color-coded sO_2 image is overlaid on top of a grayscale structural image. The lower panels show the corresponding fractional HbO_2 and Hb concentrations as well as the sO_2 value evaluated on the superior sagittal sinus (SSS). During the measurement, the pulse repetition rate was 10 Hz. The movie was created by down sampling at a ratio of 25:1.

Supplementary Video 10. Lower abdominal cavity oxygenation response of a mouse during whole-body oxygen challenge. This cross section shows the spleen, cecum, intestine, and both kidneys. The data were processed using the same method as for Fig. 4. The bottom-right panel shows the change of the signal level averaged over the entire FOV.

Supplementary Video 11. Label-free tracking of circulating melanoma tumor cells in the mouse brain *in vivo*. The light fluence on the animal skin was 8 mJ/cm^2 at 680 nm, with a pulse repetition rate of 10 Hz.

Supplementary Video 12. *In vivo* monitoring of dye perfusion in the mouse brain. The right panel shows the normalized change of the signal level averaged over the entire FOV. The dye solution (100 μL with 0.5% mass concentration) was injected through the carotid artery. The light fluence on the animal skin was 18 mJ/cm^2 at 1064 nm, with a pulse repetition rate of 50 Hz.

Supplementary Movie 13. *In vivo* label-free photoacoustic computed tomography of rat whole-body anatomy at a cross-section of lower abdominal cavity, with contrast enhancement filtering and adaptive gain compensation described in Online Methods. The entire cross-section (48 mm in width) is clearly visualized with high contrasts of rat internal organs.

References

1. Merčep, E., Burton, N.C., Claussen, J. & Razansky, D. Whole-body live mouse imaging by hybrid reflection-mode ultrasound and optoacoustic tomography. *Optics Letters* **40**, 4643-4646 (2015).
2. Dean-Ben, X.L. et al. Functional optoacoustic neuro-tomography for scalable whole-brain monitoring of calcium indicators. *Light Sci Appl.* **5**, e16201 (2016).
3. Fehm, T.F., Deán-Ben, X.L., Ford, S.J. & Razansky, D. In vivo whole-body optoacoustic scanner with real-time volumetric imaging capacity. *Optica* **3**, 1153-1159 (2016).
4. Gottschalk, S., Fehm, T.F., Deán-Ben, X.L., Tsytsarev, V. & Razansky, D. Correlation between volumetric oxygenation responses and electrophysiology identifies deep thalamocortical activity during epileptic seizures. *Neurophotonics* **4**, 011007-011007 (2017).
5. Species Specific Information: Mouse - Johns Hopkins University.
6. Yao, J. & Wang, L.V. Sensitivity of photoacoustic microscopy. *Photoacoustics* **2**, 87-101 (2014).